Structural and stoichiometric modifications in ultrathin epitaxial $BaBiO_3$ films

M. Zapf, S. Elsässer, M. Stübinger, P. Scheiderer, J. Geurts, M. Sing,* and R. Claessen
Physikalisches Institut and Würzburg-Dresden Cluster of Excellence ct.qmat, Universität Würzburg, 97074 Würzburg, Germany

(Received 25 April 2019; published 28 June 2019)

$BaBiO_3$ (BBO) is well known as the parent material for the high-T_c superconducting compounds $Ba_{1-x}K_xBiO_3$ and $BaPb_{1-x}Bi_xO_3$. In its pristine state, BBO is a charge-ordered (CO) insulator, resulting from a static breathing distortion of the BiO_6 octahedra with alternating long and short bond lengths. Recently, it has been reported that the CO state is suppressed for BBO films grown on $SrTiO_3$ (STO) below a thickness of approximately 4 nm, possibly resulting in a metallic phase. While we do confirm structural modifications in our BBO/Nb:STO samples in this thickness range by Raman spectroscopy and electron diffraction, *in situ* photoemission evidences that these changes are accompanied by a Bi deficit and that the films remain insulating. We hence conclude that, in line with previous findings for the BBO/STO interface, the thickness-controlled suppression of the CO state is not purely driven by the two-dimensional confinement but rather originates from modifications of the composition and structure inherent to the epitaxial growth of BBO on $SrTiO_3$(001).

DOI: 10.1103/PhysRevB.99.245308

I. INTRODUCTION

Confinement of perovskite oxide materials to thin films of only a few unit cell thicknesses is a unique way to alter the electronic and magnetic properties without changing the chemical composition. Intriguing examples of phase transitions in oxides upon reducing the film thickness are the metal-to-insulator transitions in vanadates, nickelates, and iridates and the change from a ferromagnetic to an antiferromagnetic state in ultrathin manganite films [1–5]. The trigger of such phenomena is commonly found in the modification of the complex interplay between the various degrees of freedom in transition metal oxides, induced by changes of, e.g., the number of nearest neighbors, the orbital order, or the magnetic coupling, by electronic reconstruction due to a polar discontinuity or subtle structural and chemical modifications at heterointerfaces. A particular interesting example of a thickness-dependent phase transition in oxides has recently been reported for thin films of the distorted perovskite bismuthate $BaBiO_3$ (BBO) deposited on $SrTiO_3$ (STO) substrates since here the confinement is claimed to lead not to an insulating—as is usually observed—but to a metallic phase [6].

BBO is the parent compound of the high-T_c superconductors $Ba_xK_{1-x}BiO_3$ and $BaPb_{1-x}Bi_xO_3$, which exhibit remarkably high critical temperatures of up to 30 K [7–10]. In its pristine bulk state the material is insulating due to the formation of charge order (CO) on the BiO_6 octahedral network of the crystal. Structurally, this CO manifests itself in an enlargement of the perovskitelike unit cell of BBO with a static breathing distortion of alternating compressed and expanded BiO_6 octahedra with Bi-O bond lengths of 2.11 and 2.29 Å, respectively. In addition, the unit cell of the room-temperature phase exhibits a monoclinic distortion stemming from a tilting of the octahedra with respect to the pseudocubic principal axes [11].

A matter of long-standing and active debate is the valence state of the Bi cations at the two structurally distinct Bi lattice sites in the CO state. In an ionic picture, the nominal valence state of Bi^{4+} in BBO is often assumed to disproportionate into Bi^{3+} and Bi^{5+} [12,13]. Photoelectron spectroscopy experiments, however, resolve only one distinct spectral line, which is often ascribed to a pure Bi^{3+} state [14,15]. While it is not clear whether photoemission can properly distinguish between Bi^{3+} and Bi^{5+} [15–18], recent theoretical studies suggest a valency of approximately Bi^{3+} at both inequivalent Bi sites in the CO phase [19]. In this case, charge neutrality is maintained through condensation of a surplus hole pair in hybridized Bi 6*s*-O 2*p*-derived molecularlike states in the ligand shell of the collapsed octahedra.

Since the static breathing distortion is linked to the CO, the structural symmetry of the BBO lattice is a footprint of the electronic charge order in the crystal. Kim *et al.* report, in a comprehensive study on epitaxial BBO on STO based on Raman spectroscopy and x-ray diffraction, that upon decreasing the film thickness to a critical value of 4–5 nm the structural symmetry of the BBO lattice is converted from the distorted perovskite to a cubic single-perovskite $Pm\bar{3}m$ phase [6]. The authors suggest that this structural phase transition arises from a suppression of the CO and the associated breathing distortion below a certain BBO film thickness. Consequently, it is speculated that with the breakdown of the charge order, BBO thin films in fact become metallic below a critical thickness [6]. However, direct experimental evidence for metallic states is lacking so far.

For this reason and in order to elucidate the physical origin of the reported structural modifications and to investigate the possible presence of a thickness-controlled insulator-to-metal transition in BBO, we carried out a complementary spectroscopic study of film-thickness-dependent modifications in our BBO thin-film samples.

*sing@physik.uni-wuerzburg.de

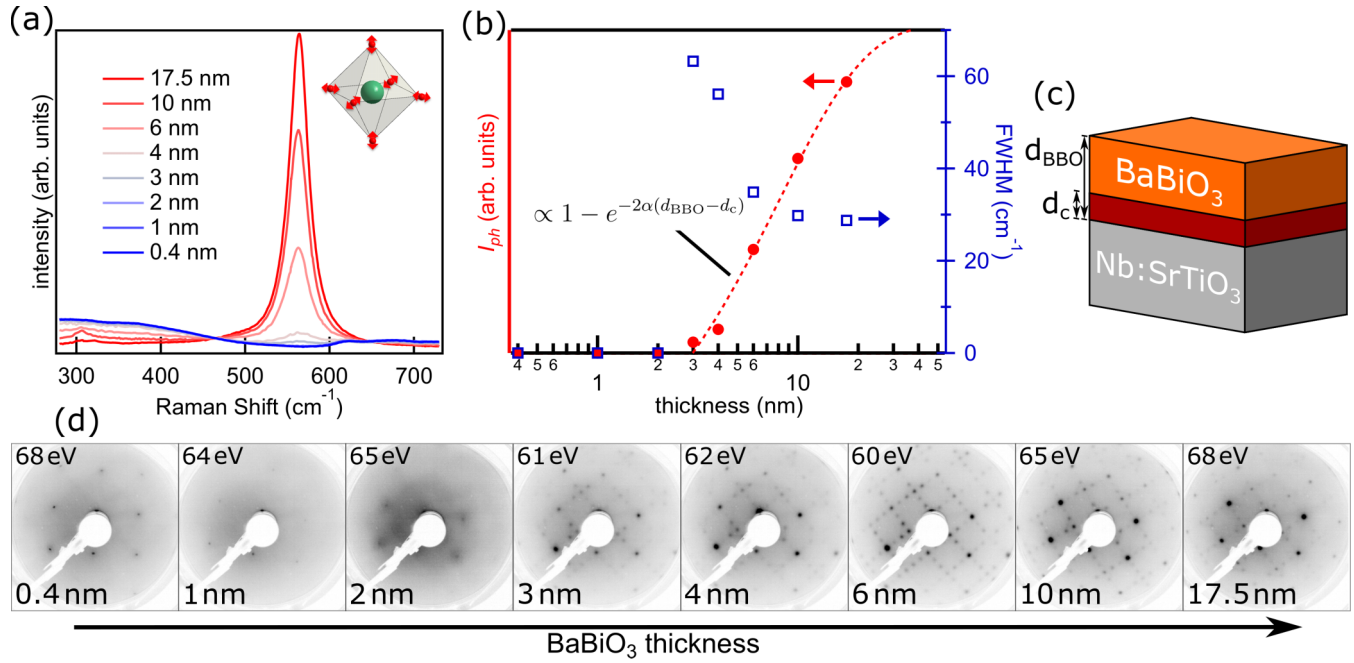

FIG. 1. (a) Raman response at a wavelength $\lambda = 633$ nm of BBO films grown on Nb:STO(001) substrates with thicknesses d_{BBO} ranging from 0.4 to 17.5 nm. (b) Relative intensity (left axis) and width (right axis) of the Raman response of the breathing phonon mode at about 565 cm^{-1} dependent on the BBO film thickness. Both quantities indicate the presence of a dead layer, not hosting the breathing phonon, below a critical thickness of 3 nm. (c) Model of the heterostructure with a layer of thickness d_c at the interface, which does not contribute to the Raman response of the film. (d) Evolution of the low-energy electron diffraction pattern of the samples dependent on the BBO thickness. For the 0.4- and 1-nm-thick samples a (1×1) symmetry of the surface lattice is observed, while thicker films exhibit a characteristic R45°$(3\sqrt{2} \times \sqrt{2})$ reconstruction. In the upper-left corner of each image the kinetic energy of the electrons is denoted.

II. EXPERIMENTAL DETAILS

To this end, we prepared a series of BBO films with thicknesses d_{BBO} ranging from 0.4 to 17.5 nm on TiO_2-terminated Nb:STO(001) substrates by pulsed laser deposition (PLD) from a stoichiometric, polycrystalline $BaBiO_3$ target. Before each sample growth, the target surface area was sanded and underwent a cleaning ablation with a fixed number of laser pulses to ensure defined and reproducible deposition conditions. All samples were grown in an oxygen background pressure of $p_{O_2} = 8 \times 10^{-2}$ mbar, at a substrate temperature of $T_S = 560\,^{\circ}$C, a laser fluency of $F_L = 1.1$ J cm^{-2}, and a laser repetition rate of 1 Hz. As shown in Appendix A, we found that a good structural order and the correct cation stoichiometry of the deposited BBO are particularly sensitive to the oxygen growth pressure, which hence has to be optimized carefully. Further details on the growth and bulk structure of the films can be found in Ref. [20].

The Raman spectroscopy measurements were performed with a confocal Raman spectrometer setup at an excitation wavelength of $\lambda = 633$ nm. The photoemission [x-ray photoelectron spectroscopy (XPS)] measurements have been conducted with a monochromatized Al K_α x-ray source in normal electron emission geometry.

III. RESULTS AND DISCUSSION

A. Raman spectroscopy and electron diffraction

To connect our study to the results of Kim *et al.* in Ref. [6], Raman spectroscopy measurements were performed on BBO films of various thicknesses. The spectra are plotted in Fig. 1(a). The most prominent feature of the Raman spectrum at an energy shift of about 565 cm^{-1} is associated with the excitation of a breathing-mode phonon as is known for BBO single crystals [cf. inset in Fig. 1(a)] [21].

Indeed, the breathing phonon dominates the Raman spectra for $d_{BBO} \geqslant 6$ nm, indicating the same lattice symmetry as for BBO single crystals in this thickness range. With decreasing film thickness, the intensity of the breathing mode declines continuously and for the thinnest films the spectra resemble that of an STO crystal [22]. A quantitative account of the intensity of the phonon excitation is obtained by fitting the spectra with Lorentzian profiles as shown in Appendix B. The resulting values I_{ph}, given by the total area of the Lorentzian, as well as the full widths at half-maximum (FWHM) of the peaks are plotted in Fig. 1(b) dependent on the film thickness.

The data can be explained by a model for the sample as shown in Fig. 1(c). The film contributes to the Raman response only beyond a critical thickness d_c, assuming that the interfacial layers may be structurally modified and therefore do not exhibit the BiO_6 breathing mode. Taking into account that the contributions from buried layers are exponentially damped, one obtains for I_{ph} the expression

$$I_{ph} \propto \int_{d_c}^{d_{BBO}} e^{-2\alpha(d_{BBO}-l)}\, dl \propto 1 - e^{-2\alpha(d_{BBO}-d_c)}, \qquad (1)$$

where α denotes the absorption coefficient for the employed laser light. This function is plotted as the dashed line in Fig. 1(b).

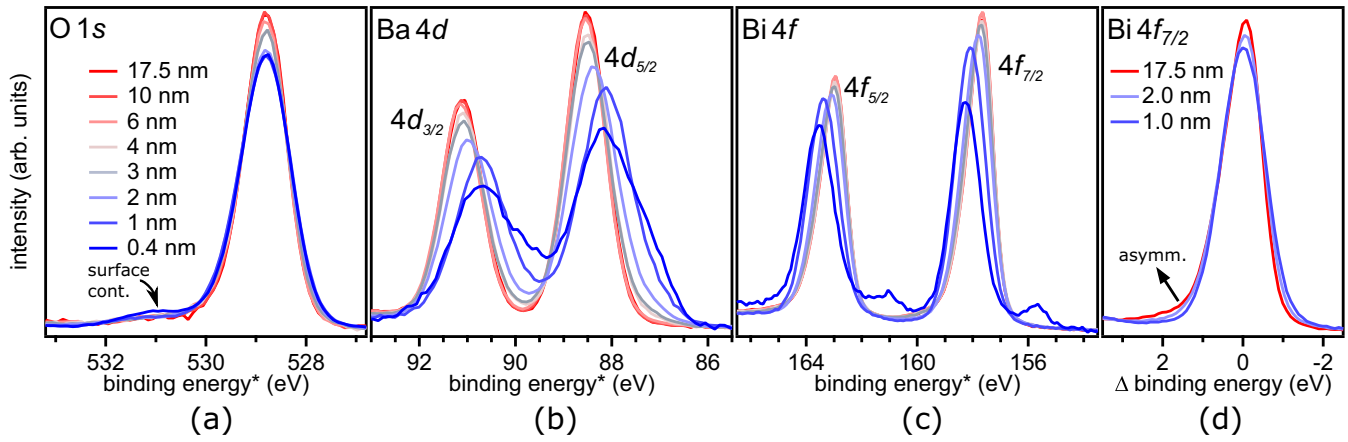

FIG. 2. (a) O 1*s*, (b) Ba 4*d*, and (c) Bi 4*f* spectra of BBO/Nb:STO samples with different film thicknesses d_{BBO}. (d) Comparison of the Bi $4f_{7/2}$ line shape of BBO films with $d_{\mathrm{BBO}} = 1$, 2, and 17.5 nm. *The binding energy is corrected for charging as described in Appendix C.

Obviously, the strength of the phonon excitation declines continuously with decreasing d_{BBO} until it vanishes at and below a critical thickness $d_c \approx 3$ nm. This absence of a *steplike* suppression of the breathing-mode intensity—as previously observed and associated with a structural first-order transition of the *entire* BBO film when d_{BBO} reaches a critical value—is the most important result of our Raman measurements. The gradual disappearance of the breathing phonon mode is accompanied by a broadening of the Raman excitation as indicated by the blue squares in Fig. 1(b). The width of the response increases from about 29 cm^{-1} for the 17.5-nm sample to 63 cm^{-1} at $d_{\mathrm{BBO}} = 3$ nm, reflecting an increasing localization of the phonon with the shrinking of the lattice volume [23,24].

A complementary confirmation of the structural modifications in the thin-film limit of our samples is obtained by low-energy electron diffraction. Figure 1(d) depicts the diffraction patterns of each sample, recorded *in situ* after film deposition at the kinetic electron energies indicated in each image.

The BBO films with thicknesses from 17.5 to 3 nm all exhibit an R45°$(3\sqrt{2} \times \sqrt{2})$ pattern as is typically observed for the surface of BBO films [20]. For $d_{\mathrm{BBO}} = 2$ nm the same reconstruction is also present, but the diffraction spots are strongly blurred, pointing towards a reduction of the size of the coherent surface lattice domains. Upon further decreasing d_{BBO} to 1 nm, the diffraction intensity widely vanishes, supporting the above results of an altered lattice structure from Raman spectroscopy. A very sharp (1×1) pattern with respect to the STO surface unit cell becomes visible at $d_{\mathrm{BBO}} = 0.4$ nm. This pattern either stems indeed from a quadratic symmetry of the surface lattice of the films or, more likely, originates from electrons probing the underlying STO substrate through the thin or even incomplete film layer.

As clarified in our preceding study [20] by means of transmission electron microscopy, a structurally distinct interfacial layer of about 2-nm thickness relieves the mismatch strain between the substrate and the film at the interfaces of BBO/STO heterostructures [20]. Beyond this, the film structure accords with that of bulk perovskitelike BBO. As shown here, these structurally different interfacial film layers are also present when the deposition process is stopped within the growth of the first 2 nm of the film. Hence, we suggest that the suppression of the phonon mode at $d_{\mathrm{BBO}} \leqslant 2$ nm has to be traced back to the lattice modifications at the interface. The interfacial lattice, due to its disturbed structure, does not host the breathing phonon and consequently does not contribute to the BBO Raman response, as is assumed in our model above, explaining the observed critical thickness behavior for the excitation of the breathing phonon.

B. Core-level photoemission

In order to correlate the structural modifications with the electronic structure of the BBO films, we employ *in situ* photoemission. To this end, the samples were transferred to an XPS analysis chamber under ultrahigh vacuum conditions. Figures 2(a)–2(c) show a comparison of the O 1*s*, Ba 4*d*, and Bi 4*f* core-level spectra for the different BBO film thicknesses. All depicted spectra are measured in normal emission geometry and are normalized to the same integral intensity.

As detailed in Appendix C, we observe a static charging of the samples during irradiation with x-ray photons which is favored by the specific band alignment at the interface of BBO and Nb:STO. As a consequence, a straightforward determination of the position of the chemical potential of the samples by XPS is not possible. In order to compare the spectra of different samples, the binding energy scale for each measurement is calibrated by fixing the position of the O 1*s* core-level line to a value of 528.8 eV (see Appendix C for details).

A weak shoulder is visible on the high-binding-energy side of the O 1*s* core level. Since this feature is more pronounced in more surface sensitive measurement geometries, i.e., at higher emission angles (not shown), it is assigned to surface contaminations from the residual gas. Note that the broadening of the O 1*s* line for $d_{\mathrm{BBO}} < 6$ nm likely stems from a superposition of differing spectral contributions from the substrate, the interface film layer, and the overlying undisturbed bulk-like BBO film.

The Ba 4*d* core level of the samples with $d_{\mathrm{BBO}} > 6$ nm in Fig. 2(b) resembles the single spin-orbit split doublet expected for pristine BBO, indicating that Ba occupies solely the *A* lattice site of the perovskite phase of BBO [18]. Upon reducing the film thickness below 6 nm, the peak maximum

shifts gradually to lower binding energies by up to 380 meV. Simultaneously, the core level broadens substantially, from an FWHM of 0.95 eV for $d_{\mathrm{BBO}} = 17.5$ nm to 1.71 eV, when reducing d_{BBO} to 0.4 nm. With the only stable oxidation state of Ba being Ba^{2+}, the observed changes are likely associated with a distorted or inhomogeneous local environment of the Ba cations in the thinnest films, presumably reflecting the layerwise modifications of the structure in the interfacial layers of the BBO/Nb:STO heterostructure [20].

Pronounced changes are also detected in the Bi $4f$ spectra depicted in Fig. 2(c). For film thicknesses $\geqslant$4 nm the core-level doublet is virtually thickness independent and agrees with the line shape observed for BBO single crystals [18]. For these samples, exemplarily shown in Fig. 2(d), which compares the sample with $d_{\mathrm{BBO}} = 17.5$ nm to those with film thicknesses of 2.0 and 1.0 nm, the Bi $4f$ lines exhibit an asymmetry toward higher binding energies that is characteristic for the BBO bulk phase. The asymmetric shape has been associated in the literature with an energy loss originating from interband transitions across the CO band gap or low-energy plasmon excitations [18,25,26]. For the thinnest films, with $d_{\mathrm{BBO}} \leqslant 2$ nm, the asymmetry is not present [cf. Fig. 2(d)] and the Bi $4f$ core level is shifted to higher binding energies, highlighting the distinction of the thin BBO samples from the thicker films with regard to the electronic properties.

The spectrum of the $d_{\mathrm{BBO}} = 0.4$ nm sample in Fig. 2(c) exhibits a small additional doublet line shifted by about 2.6 eV toward lower binding energies with respect to the main line. This additional spectral weight increases with the time of x-ray irradiation, indicating an instability of the atomic bonds in bismuthate films with thicknesses in the range of one unit cell. Due to the size of the energetic shift, we tentatively assign it to elemental Bi generated from a photon-induced conversion of oxidized Bi [17].

Besides the noticeable changes in the shape of the core-level spectra, also the elemental composition of the samples exhibits a significant thickness dependence. A relative measure for the cation stoichiometry of the samples is obtained from the ratio of the spectral intensities of the Ba $4d$ and Bi $4f$ core levels [red-shaded areas in Fig. 3(a)] after subtraction of the secondary electron background (blue-shaded areas). The ratio is calibrated to an absolute value for the cation off-stoichiometry of the thin films x based on the formula $Ba_{1+x}Bi_{1-x}O_y$ by means of a reference measurement of Ba $4d$ and Bi $4f$ on the stoichiometric BBO target material, for which $x = 0$ is assumed. The upper panel in Fig. 3(b) shows the resulting values of x dependent on the film thickness, while the lower panel displays the binding energy position of the Bi $4f_{7/2}$ line extracted from Fig. 2(c).

Apparently, while the cation stoichiometry of the thickest films is close to $x = 0$, for $d_{\mathrm{BBO}} < 6$ nm the samples exhibit a lower Bi-to-Ba ratio, with an increase of x up to 0.3 for the sample with $d_{\mathrm{BBO}} = 0.4$ nm. In parallel to this off-stoichiometry, the binding energy of the Bi $4f_{7/2}$ core level shifts towards higher values.

As Ba is bound to its oxidation state Ba^{2+}, additional holes have to be compensated in Ba-rich films with $d_{\mathrm{BBO}} < 6$ nm to maintain charge neutrality. This could be achieved through an adjustment of the oxygen stoichiometry y, i.e., oxygen vacancies, or by lifting the oxidative state of the multivalent

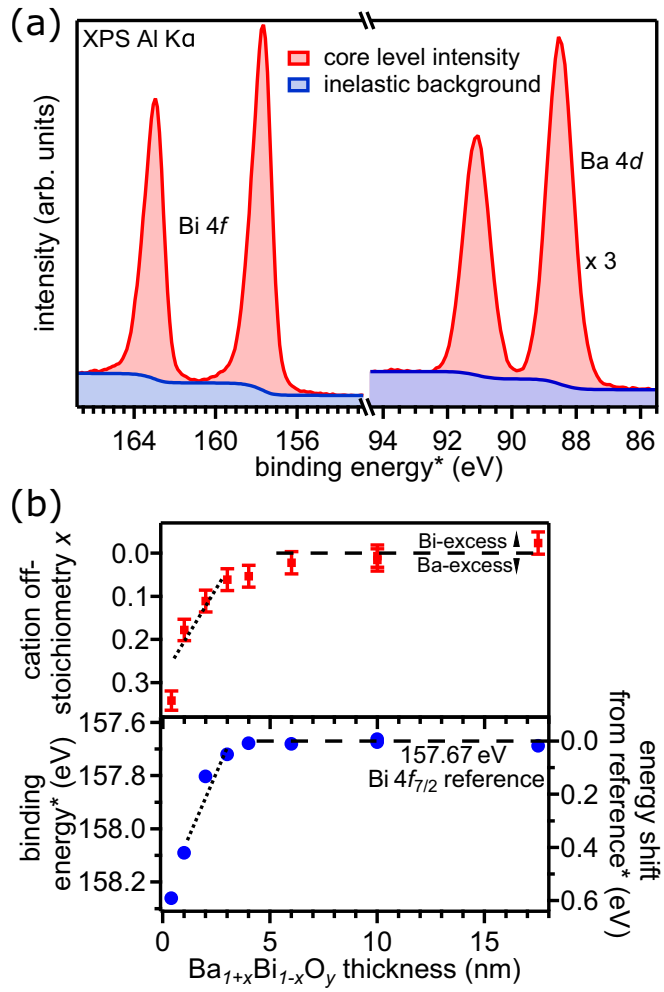

FIG. 3. (a) Evaluation of the integrated intensities of the Bi $4f$ and Ba $4d$ core levels for determination of the cation stoichiometry. (b) Upper graph: Cation off-stoichiometry x dependent on the film thickness. x is obtained by a calibration of the ratio of the Bi $4f$ and Ba $4d$ core-level area intensities to that of a reference measurement on the stoichiometric BBO target material ($x = 0$). Experimental uncertainties are indicated by error bars. Lower graph: Binding energy of Bi $4f$ (left axis) and energy shift relative to the reference position (right axis) dependent on the film thickness. Dotted lines are guides for the eye. *The binding energy is corrected for charging as described in Appendix C.

element Bi towards Bi^{5+}. The latter scenario was suggested by Itoh *et al.* to take place in Bi-deficient bulk crystal samples of BBO [27]. In this fully ionic picture, the increase in x is expected to result in a concomitant increase in spectral weight in the Bi core-level spectra associated with Bi^{5+}, similarly to what is observed in many doped $3d$ transition metal oxide systems [28–30]. However, such changes in the Bi valence are not detected in the present measurements, since only a single Bi doublet is observed for all samples. Still, as mentioned before, the binding energy split between the spectral components of different oxidation states of Bi might just be too small to be resolved [17,18].

Alternatively, the notion of integer oxidation numbers may not be a meaningful concept at all due to the rather covalent

nature of the Bi-O bond. In this case, the smaller number of electrons on the Bi-O sublattice with increasing x could just result in a rigid shift of the Bi $4f$ core level to higher binding energies, as observed here.

A conceivable cause for the deviation of the thin-film composition could be a modification of the target stoichiometry during PLD growth. To exclude such effects, the target area used was ablated for cleaning before the actual film deposition with a multiple of the laser pulses (i.e., >400 pulses) as used to grow the thin films (20 pulses $\widehat{=}$ 1 nm). As an additional cross-check, two 1-nm-thick films were grown in direct succession with ablation from the same target spot and another 400 laser pulses in between. Indeed, the small change in x of about 0.05 is measured for these two samples, pointing towards a change in the target stoichiometry during growth. However, the absolute difference is too small to explain the differences in $\Delta x > 0.3$ between the 0.4-nm- and the >6-nm-thick films, ruling out a target degradation scenario as the main reason for the strong deviations of the cation stoichiometry in ultrathin BBO.

A similar stoichiometric alteration of the initially deposited layers towards a bismuth deficit was observed before in molecular beam epitaxy of BBO films on MgO substrates [31]. In a consecutive study, the same authors found that the sticking coefficient of Bi increases significantly when a layer of Ba has previously been deposited underneath [32]. The alteration of the cation stoichiometry observed in our experiments thus likely is caused by general thermodynamics, closely related to the volatility of bismuth, rather than being of specific PLD process-related origin. It is speculated that the tendency of reevaporation of Bi during the initial growth is related to the weak stability of the crystalline bonding environment of Bi, as also reflected in the irradiation-induced changes in the Bi $4f$ core-level line of the $d_{\mathrm{BBO}} = 0.4$ nm sample mentioned above.

C. Valence band photoemission

To answer the question whether an insulator-to-metal transition occurs when the film thickness is decreased below the critical value we also measured valence band spectra by XPS dependent on the BBO film thickness [see Fig. 4(a)]. Again, the relative binding energy scale is calibrated as described in Appendix C. We remark that the spectra of the samples with $d_{\mathrm{BBO}} < 6$ nm are a superposition of the valence band spectra of the film and the STO substrate, which is the main origin of the changes in the spectral shape at binding energies higher than 2 eV with decreasing film thickness.

The valence band of the thick films resembles that of bulk BBO [15,18,33], where the tail of a characteristic steplike feature at the valence band edge touches the chemical potential. However, no Fermi edge is visible, signaling the semiconducting nature of the material. When the BBO film thickness is decreased to $d_{\mathrm{BBO}} < 3$ nm, the steplike feature vanishes. This is also manifest in Fig. 4(b), which shows the decomposition of the valence band spectrum of the sample with $d_{\mathrm{BBO}} = 1$ nm into the valence band spectrum of a bare Nb:STO substrate (dotted blue line) and that of a 10-nm-thick BBO film (dotted green line). Apparently, the states forming the steplike feature [arrow in Fig. 4(b)] are not occupied in the samples with $d_{\mathrm{BBO}} < 3$ nm, possibly due to the reduced number of valence electrons in the Bi-deficient system, or in fact not present in the electronic structure of the structurally modified lattice. Consequently, it can be ruled out that the absence of the CO phase in the thin-film limit is accompanied by a closing of the CO band gap, as suggested by the authors of Ref. [6]. In other words, the BBO films do not turn metallic in the thin-film limit.

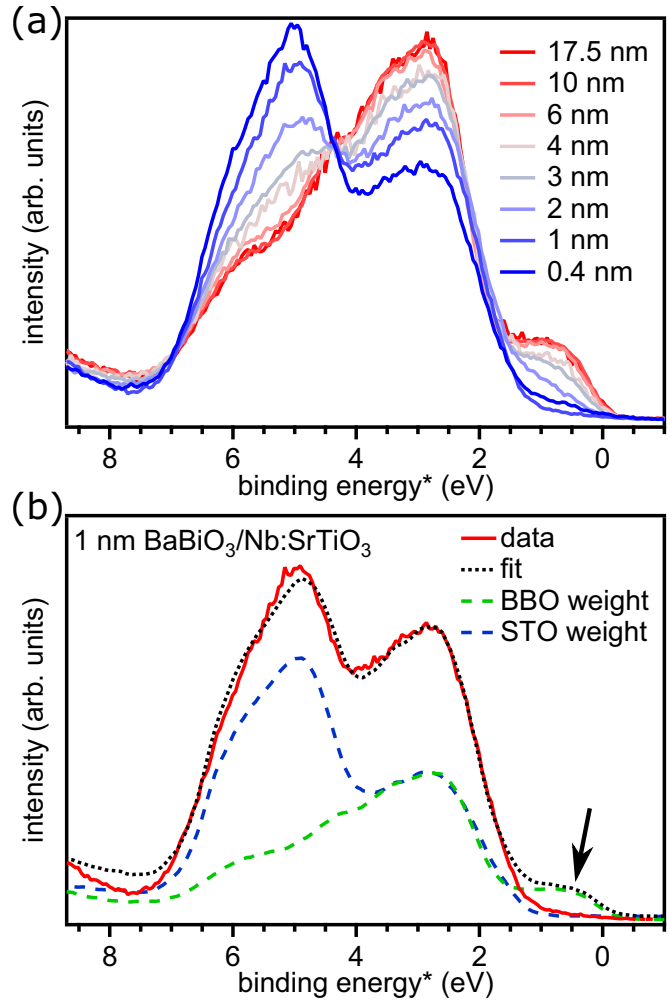

FIG. 4. (a) XPS valence band spectra of samples with different BBO thicknesses. The transition from the STO-dominated valence band for thin films to the BBO valence band at larger film thicknesses is illustrated. (b) Exemplary decomposition of the valence band of the 1-nm-thick BBO sample into the valence band spectra of a bare Nb:STO substrate and a 10-nm-thick BBO film. The typical steplike valence band onset (arrow) is missing for samples with $d_{\mathrm{BBO}} < 3$ nm. *The binding energy is corrected for charging as described in Appendix C.

IV. CONCLUSION

We have presented an investigation of the structural and spectroscopic properties of BBO thin films dependent on their thickness. In accordance with Ref. [6], Raman spectroscopy and low-energy electron diffraction point towards a structural alteration of the BBO lattice in the thin-film limit below a

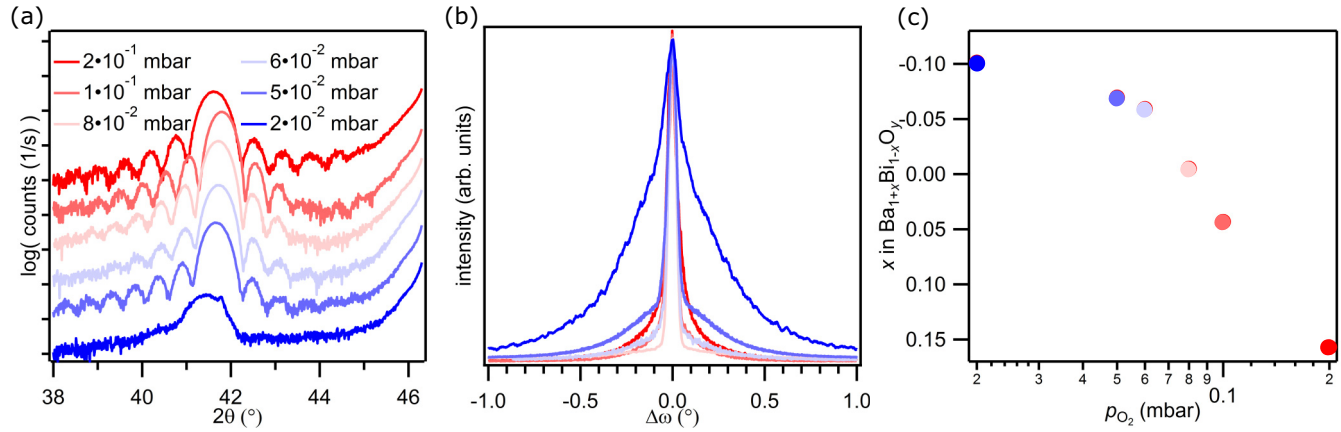

FIG. 5. Properties of BBO thin films deposited in different oxygen background pressures between $p_{O_2} = 2 \times 10^{-2}$ mbar and $p_{O_2} = 2 \times 10^{-1}$ mbar. (a) ω-2θ scans around the BBO(002) diffraction peak. (b) Corresponding rocking curves of the BBO(002) peak. (c) Cation off-stoichiometry x evaluated in the same way as in Fig. 3.

thickness of $d_{BBO} = 3$ nm. However, no evidence is found for a spontaneous structural transition, but rather a *gradual* vanishing of the BBO bulk phonon Raman response with decreasing film thickness is observed. The film volume below a thickness of 3 nm does not contribute to the Raman signal. Such a dead layer is in line with the initial growth of a film lattice that is structurally different from that of bulk BBO, persists at the interface also during ongoing deposition, and eventually forms the interfacial layer in the BBO/STO heterostructure as reported in Ref. [20]. Employing XPS, it is deduced that the structural modifications are attended by a distinct Bi deficit in the initially formed film layers. The connected thickness-dependent differences in the local lattice environments of the Ba and Bi cations entail pronounced changes in the Bi 4f and Ba 4d core-level spectra. Accordingly, the valence states of the samples with $d_{BBO} < 3$ nm are also modified in comparison to those of thicker BBO films. All investigated films remain insulating.

In summary, the interpretation of a thickness-controlled vanishing of the BiO_6 breathing phonon as a breakdown of the CO state, caused solely by the reduction of the dimensionality, falls short for our $BaBiO_3$ thin films. Our measurements rather demonstrate that the epitaxy-related interfacial modifications, including an altered stoichiometry in proximity to the interface, underlie the film-thickness-dependent modifications observed in the BBO/STO system. Our results emphasize the importance of a comprehensive review of structure, chemical composition, and electronic properties when evaluating the origin of thickness-dependent phenomena in oxide thin films.

ACKNOWLEDGMENTS

The authors acknowledge financial support from the Bundesministerium für Bildung und Forschung (BMBF) under Grant Nos. 05K13WW1 and 05K16WWA and the Deutsche Forschungsgemeinschaft (DFG, German Research Foundation) under Grant Nos. Ge1855/10-2 and CL124/14-2 as well as through SFB 1170 (Project I.D. 258499086) and the Würzburg-Dresden Cluster of Excellence on Complexity and Topology in Quantum Matter—*ct.qmat* (EXC 2147, Project I.D. 39085490).

APPENDIX A: OPTIMIZATION OF THE OXYGEN BACKGROUND PRESSURE FOR $BaBiO_3$ GROWTH

In order to obtain the most favorable conditions for the deposition of BBO thin films in the present study, we performed a systematic empirical optimization of the three growth parameters T_S, p_{O_2}, and F_L. To this end, three individual sets of BBO thin-film samples were prepared. In each sample set one particular growth parameter was varied, while the other two parameters were kept at a fixed value. The samples were examined by x-ray diffraction, and the cation stoichiometry was determined by means of XPS in analogy to Fig. 3.

Figure 5 exemplarily shows the data used to determine the oxygen growth pressure. Figure 5(a) depicts ω-2θ scans around the BBO(002) diffraction peak (pseudocubic notation) for films with thicknesses in the range of 16–19 nm, grown at oxygen pressures of $p_{O_2} = 2 \times 10^{-2}$ to 2×10^{-1} mbar, at $T_S = 560\,^{\circ}$C, and $F_L = 1.1$ J cm^{-2}. Apparently, indicated by the nicely visible thickness fringes, a well-ordered epitaxial BBO film is obtained for all growth pressures above $p_{O_2} = 2 \times 10^{-2}$ mbar. In contrast, the lack of thickness fringes for the sample deposited at $p_{O_2} = 2 \times 10^{-2}$ mbar already signals a worsening of the lattice order for too low oxygen background pressures.

Epitaxial BBO thin films commonly consist of individual crystallites that are slightly tilted with respect to each other. This mosaic structure is essentially related to the density of dislocations and other defects in the lattice and can be probed by so-called rocking scans of the film Bragg peaks. The FWHM of the diffraction peaks in such rocking scans serves as a relative measure for the defect density of the films. Figure 5(b) depicts the rocking curves of the BBO(002) reflexes of the present sample set in Fig. 5(a). Apparently, the rocking curves exhibit a significant dependence on the oxygen growth pressure, with the narrowest peak being observed for the $p_{O_2} = 8 \times 10^{-2}$ mbar sample.

The main reason for the growth pressure dependence of the defect density is found when analyzing the stoichiometry of the films. As deducible from Fig. 5(c), the cation off-stoichiometry x of the samples also exhibits a strong dependence on the oxygen growth pressure and is minimal

for $p_{O_2} = 8 \times 10^{-2}$ mbar. A deviation from the nominal 1:1 ratio of Ba and Bi in the films obviously increases the defect density and misorientation of crystallites in the BBO film.

Strong dependencies of the cation stoichiometry of the deposited material on the growth pressure are a commonly observed phenomenon for PLD of multicomponent oxides at deposition pressures above 10^{-2} mbar [34–36]. While at lower pressures the plasma plume expands virtually freely in the vacuum chamber, in the pressure regime above 10^{-2} mbar collisions with the background gas become important. These interactions depend on the mass and scattering cross sections of the particular plume species and often result in modifications of the stoichiometry of the material condensing on the substrate surface. Additionally, the concurrent thermalization of the species in the plasma plume at higher pressures reduces possible resputtering of deposited material from the substrate, which often affects the film composition at lower growth pressures.

Conclusively, on the basis of the results in Figs. 5(b) and 5(c), a pressure of $p_{O_2} = 8 \times 10^{-2}$ mbar was chosen for the preparation of the thin films in this study.

APPENDIX B: ANALYSIS OF THE BREATHING PHONON RAMAN RESPONSE

The Raman response of the breathing phonon of the thickness series of $BaBiO_3$/Nb:$SrTiO_3$ samples is evaluated quantitatively by fitting the breathing phonon excitation at 565 cm^{-1}. The spectrum of the sample with a thickness of 0.4 nm [blue line in Fig. 1(a)] shows no indications of phonon excitations from the BBO film but closely resembles the Raman response of an STO crystal. STO in its ideal cubic room-temperature phase is expected to have no first-order Raman active modes. The spectral contributions below about 400 cm^{-1} and above about 650 cm^{-1}, constituting the STO response, are due to second-order Raman scattering processes [22]. The peak of the BBO breathing mode occurs at the minimum in between and is separated from the background intensity by subtracting the spectrum for the 0.4-nm-thick sample from each spectrum of the samples with higher BBO thicknesses. This procedure is, in particular, necessary to properly evaluate the spectral form of the rather weak breathing phonon response of BBO films with $d_{BBO} = 3$ and 4 nm. As can be seen from the tail regions in Figs. 6(b)–6(f), the subtraction in fact slightly overcorrects the contributions from the substrate to the spectra but otherwise results in phonon peak shapes which can be reasonably evaluated also for samples with $d_{BBO} \leqslant 4$ nm.

Eventually, the spectra in Figs. 6(b)–6(f) were fitted over the energy range between 465 and 650 cm^{-1} by Lorentzian lines. The obtained values for the absolute area of the Lorentzians and their FWHM dependent on the BBO film thickness are displayed in Fig. 1(b).

APPENDIX C: BAND ALIGNMENT AT THE $BaBiO_3$/Nb:$SrTiO_3$ INTERFACE

Figure 7(a) compares, shown by colored lines, the O 1*s* core-level spectra of a BBO film grown on Nb:STO, measured with an Al K_α x-ray tube at four emission currents, i.e., x-ray

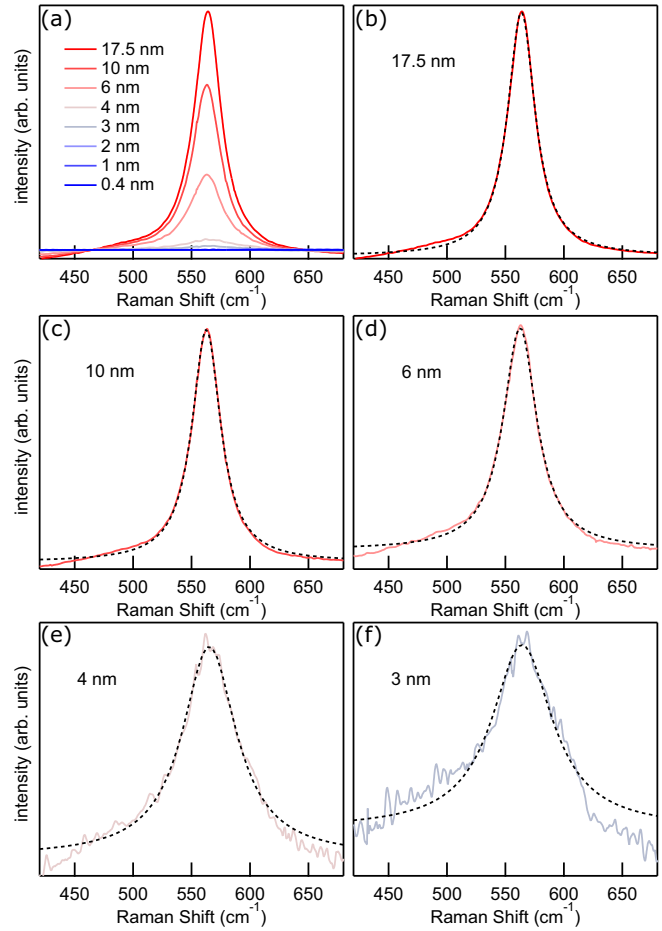

FIG. 6. (a) Background-subtracted Raman spectra of the breathing phonon excitation for different film thicknesses. (b–f) Lorentzian fits of the breathing phonon response of samples with $d_{BBO} \geqslant 3$ nm. Each ordinate scaling is normalized to the intensity of the peak maximum.

intensities. While for a fixed x-ray intensity the kinetic energy position of the core level is stable during irradiation, it shifts to lower kinetic energies with increasing x-ray intensity due to a retardation of the photoelectrons as a result of sample charging. Obviously, the charge being emitted through the photoemission process is not fully replenished by grounding the substrate back. The Nb:STO substrate itself, as an *n*-doped crystal with metallic conduction, provides a good electrical contact to the sample holder. BBO, on the other hand, is expected to be intrinsically insulating. Nevertheless, the kinetic energy positions of the film core-level lines exhibit only minor variations between BBO/Nb:STO samples with different BBO thicknesses (not shown). This points towards some residual conductivity in the BBO films, possibly related to defect states, and rules out the limited film conductivity as a decisive factor for the observed charging. We thus are led to conclude that impeded transport of electrons between the Nb:STO substrate and the BBO film across the interface is responsible for the charging. As explained in the following, the reason can be found in the particular arrangement of the electronic bands at the interface.

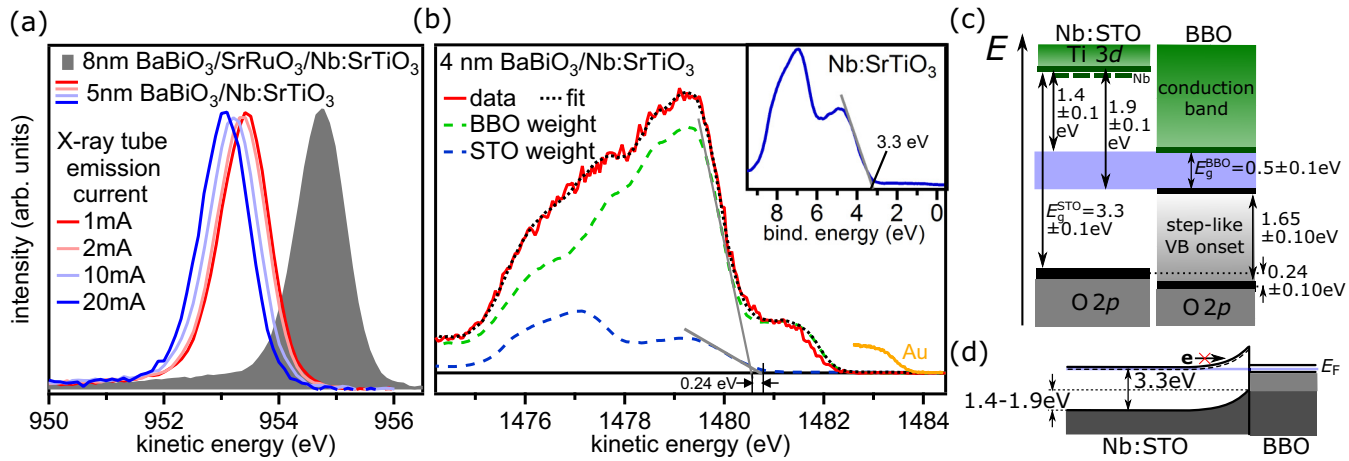

FIG. 7. (a) O 1*s* core-level spectra of a BBO film on Nb:STO dependent on the emission current of the Al K_α x-ray tube. (b) Decomposition of the valence band of a sample with a 4-nm-thick BBO film. (c) Band alignment at the $BaBiO_3$/Nb:$SrTiO_3$ interface as derived from (b). (d) Upward band bending towards the interface in the Nb:STO substrate, hampering electron transfer across the interface into the film.

We determine the band alignment at the heterointerface based on valence band photoemission, as illustrated exemplarily for the BBO/Nb:STO sample with $d_{BBO} = 4$ nm in Fig. 7(b). This film thickness is small enough that the valence band spectrum, measured with Al K_α radiation, is a superposition of spectra originating from both the substrate and the BBO overlayer. The spectrum is decomposed into the two contributions by fitting a sum of two reference spectra of the valence bands of BBO and Nb:STO. The latter is measured on a bare Nb:STO substrate and is plotted in the inset in Fig. 7(b). As a reference for the film valence band the XPS data for a 10-nm-thick BBO film is used. The fit allows for both a scaling in intensity and a shift in kinetic energy of the reference spectra. The orange line in Fig. 7(b) indicates the Fermi edge of a Au reference to point out the position of the chemical potential (without charging).

Indicated by the gray lines in Fig. 7(b), the decomposition of the spectrum of the heterostructure yields a relative band offset of 0.24 eV, given by the energy difference between the leading O 2*p*–derived valence band edges of BBO and Nb:STO. With this result and taking into account the band gaps of BBO ($E_g^{BBO} = 0.5$ eV [37]) and STO ($E_g^{STO} = 3.3$ eV [38]), the band diagram of the heterointerface in Fig. 7(c) can be deduced. The position of the Fermi energy in the system cannot be determined directly due to the unknown size of the charging potential. However, in Fig. 7(b) no Fermi cutoff is discernible at the characteristic steplike onset of the BBO valence band, which constitutes the lower edge of the CO band gap of BBO, and also no indications of occupied states in the CO band gap itself. Hence, we conclude that the chemical potential is located somewhere inside the blue-shaded band gap region of BBO in Fig. 7(c). The green areas in Fig. 7(c) accordingly mark the unoccupied states.

From the band scheme in Fig. 7(c) we infer that the chemical potential in the interfacial substrate layers of the BBO/Nb:STO heterostructure is located 1.4–1.9 eV below the conduction band in comparison to the Nb:STO bulk. Thus, in the vicinity of the interface the bands of Nb:STO are bent upwards, as schematically shown in Fig. 7(d), forming a Schottky-like potential barrier in the substrate. This barrier, with an energetic height of 1.4–1.9 eV, restricts a direct electron transport from the grounded back of the substrate to the probed sample surface and provides a viable explanation for the charging during photoemission measurements.

Due to the relatively sharp line shape of the O 1*s* core level, which is almost independent of the film thickness [cf. Fig. 2(a)], it is utilized as a reference for calibration of a relative binding energy scale for XPS measurements of different BBO/Nb:STO samples. Accordingly, the binding energy of all photoemission measurements on the BBO/Nb:STO samples (marked by an asterisk) reported in this publication are calibrated by aligning the respective O 1*s* lines to a fixed reference value. This procedure allows us to directly compare XPS spectra of the various BBO/Nb:STO samples with each other on a common energy scale, independent of the energy shift caused by the irradiation-induced charging. As a reference energy we utilized the peak maximum of the O 1*s* core level of a BBO film deposited on a Nb:STO(001) substrate with an 8-unit-cell-thick metallic $SrRuO_3$ (SRO) buffer layer [gray-shaded spectrum in Fig. 7(a)]. By introducing the SRO layer into the heterostructure, charging of the BBO films during x-ray irradiation is readily avoided and the chemical potential of the films is pinned in close proximity to the steplike valence band onset in the CO band gap [39].

[1] K. Yoshimatsu, T. Okabe, H. Kumigashira, S. Okamoto, S. Aizaki, A. Fujimori, and M. Oshima, Phys. Rev. Lett. **104**, 147601 (2010).

[2] K. Yoshimatsu, K. Horiba, H. Kumigashira, T. Yoshida, A. Fujimori, and M. Oshima, Science **333**, 319 (2011).

[3] R. Scherwitzl, S. Gariglio, M. Gabay, P. Zubko, M. Gibert, and J.-M. Triscone, Phys. Rev. Lett. **106**, 246403 (2011).

[4] P. Schütz, D. Di Sante, L. Dudy, J. Gabel, M. Stübinger, M. Kamp, Y. Huang, M. Capone, M.-A. Husanu, V. N. Strocov,

G. Sangiovanni, M. Sing, and R. Claessen, Phys. Rev. Lett. **119**, 256404 (2017).
[5] M. Huijben, L. W. Martin, Y.-H. Chu, M. B. Holcomb, P. Yu, G. Rijnders, D. H. A. Blank, and R. Ramesh, Phys. Rev. B **78**, 094413 (2008).
[6] G. Kim, M. Neumann, M. Kim, M. D. Le, T. D. Kang, and T. W. Noh, Phys. Rev. Lett. **115**, 226402 (2015).
[7] A. W. Sleight, J. L. Gillson, and P. E. Bierstedt, Solid State Commun. **17**, 27 (1975).
[8] L. F. Mattheiss, E. M. Gyorgy, and D. W. Johnson Jr., Phys. Rev. B **37**, 3745(R) (1988).
[9] R. J. Cava, B. Batlogg, J. J. Krajewski, R. Farrow, L. W. Rupp Jr., A. E. White, K. Short, W. F. Peck, and T. Kometani, Nature **332**, 814 (1988).
[10] L. F. Schneemeyer. J. K. Thomas, T. Siegrist, B. Batlogg, L. W. Rupp, R. L. Opila, R. J. Cava, and D. W. Murphy, Nature **335**, 421 (1988).
[11] B. J. Kennedy, C. J. Howard, K. S. Knight, Z. Zhang, and Q. Zhou, Acta Crystallogr. B **62**, 537 (2006).
[12] D. E. Cox and A. W. Sleight, Solid State Commun. **19**, 969 (1976).
[13] C. M. Varma, Phys. Rev. Lett. **61**, 2713 (1988).
[14] M. S. Hegde, P. Barboux, C. C. Chang, J. M. Tarascon, T. Venkatesan, X. D. Wu, and A. Inam, Phys. Rev. B **39**, 4752(R) (1989).
[15] Z.-X. Shen, P. A. P. Lindberg, B. O. Wells, D. S. Dessau, A. Borg, I. Lindau, W. E. Spicer, W. P. Ellis, G. H. Kwei, K. C. Ott, J.-S. Kang, and J. W. Allen, Phys. Rev. B **40**, 6912 (1989).
[16] G. K. Wertheim, J. P. Remeika, and D. N. E. Buchanan, Phys. Rev. B **26**, 2120(R) (1982).
[17] W. E. Morgan, W. J. Stec, and J. R. Van Wazer, Inorg. Chem. **12**, 953 (1973).
[18] M. Nagoshi, T. Suzuki, Y. Fukuda, K. Ueki, A. Tokiwa, M. Kiruchi, Y. Syono, and M. Tachiki, J. Phys.: Condens. Matter **4**, 5769 (1992).
[19] K. Foyevtsova, A. Khazraie, I. Elfimov, and G. A. Sawatzky, Phys. Rev. B **91**, 121114(R) (2015).
[20] M. Zapf, M. Stübinger, L. Jin, M. Kamp, F. Pfaff, A. Lubk, B. Büchner, M. Sing, and R. Claessen, Appl. Phys. Lett. **112**, 141601 (2018).
[21] S. Tajima, M. Yoshida, N. Koshizuka, H. Sato, and S. Uchida, Phys. Rev. B **46**, 1232 (1992).
[22] W. G. Nilsen and J. G. Skinner, J. Chem. Phys. **48**, 2240 (1968).
[23] H. Richter, Z. P. Wang, and L. Ley, Solid State Commun. **39**, 625 (1981).
[24] I. H. Campbell and P. M. Fauchet, Solid State Commun. **58**, 739 (1986).
[25] T. J. Wagener, H. M. Meyer, D. M. Hill, Y. Hu, M. B. Jost, J. H. Weaver, D. G. Hinks, B. Dabrowski, and D. R. Richards, Phys. Rev. B **40**, 4532 (1989).
[26] M. Qvarford, V. G. Nazin, A. A. Zakharov, M. N. Mikheeva, J. N. Andersen, M. K.-J. Johansson, G. Chiaia, T. Rogelet, S. Soderholm, O. Tjernberg, H. Nylen, I. Lindau, R. Nyholm, U. O. Karlsson, S. N. Barilo, and S. V. Shiryaev, Phys. Rev. B **54**, 6700 (1996).
[27] M. Itoh, T. Sawada, R. Liang, H. Kawaji, and T. Nakamura, J. Solid State Chem. **87**, 245 (1990).
[28] M. Sing, G. Berner, K. Goß, A. Müller, A. Ruff, A. Wetscherek, S. Thiel, J. Mannhart, S. A. Pauli, C. W. Schneider, P. R. Willmott, M. Gorgoi, F. Schäfers, and R. Claessen, Phys. Rev. Lett. **102**, 176805 (2009).
[29] J. Gabel, M. Zapf, P. Scheiderer, P. Schütz, L. Dudy, M. Stübinger, C. Schlueter, T.-L. Lee, M. Sing, and R. Claessen, Phys. Rev. B **95**, 195109 (2017).
[30] P. Scheiderer, M. Schmitt, J. Gabel, M. Zapf, M. Stübinger, L. Dudy, C. Schlueter, T.-L. Lee, M. Sing, and R. Claessen, Adv. Mater. **30**, 1706708 (2018).
[31] M. G. Norton, E. S. Hellman, E. H. Hartford Jr., and C. B. Carter, J. Cryst. Growth **113**, 716 (1991).
[32] M. G. Norton, E. S. Hellman, E. H. Hartford Jr., and C. B. Carter, Physica C **205**, 347 (1993).
[33] R. Itti, I. Tomeno, K. Ikeda, K. Tai, N. Koshizuka, and S. Tanaka, Phys. Rev. B **43**, 435 (1991).
[34] J. Schou, Appl. Surf. Sci. **255**, 5191 (2009).
[35] P. Orgiani, R. Ciancio, A. Galdi, S. Amoruso, and L. Maritato, Appl. Phys. Lett. **96**, 032501 (2010).
[36] I. Marozau, P. T. Das, M. Döbeli, J. G. Storey, M. A. Uribe-Laverde, S. Das, C. Wang, M. Rössle, and C. Bernhard, Phys. Rev. B **89**, 174422 (2014).
[37] H. Uwe and K. Tachibana, in Advances in Superconductivity VII. *Proceedings of the 7th International Symposium on Superconductivity*, edited by K. Yamafuchi and T. Morishita (Springer, Tokyo, 1995), p. 165.
[38] S. A. Chambers, T. Droubay, T. C. Kaspar, M. Gutowski, and M. van Schilfgaarde, Surf. Sci. **554**, 81 (2004).
[39] N. C. Plumb, D. J. Gawryluk, Y. Wang, Z. Ristić, J. Park, B. Q. Lv, Z. Wang, C. E. Matt, N. Xu, T. Shang, K. Conder, J. Mesot, S. Johnston, M. Shi, and M. Radović, Phys. Rev. Lett. **117**, 037002 (2016).